

Near-Infrared and X-Ray Observations of XSS J12270–4859

Kei SAITOU,^{1,2} Masahiro TSUJIMOTO,¹ Ken EBISAWA,^{1,2} Manabu ISHIDA,¹ Koji MUKAI,³
Takahiro NAGAYAMA,⁴ Shogo NISHIYAMA,⁵ and Poshak GANDHI¹

¹*Japan Aerospace Exploration Agency, Institute of Space and Astronautical Science,
3-1-1 Yoshinodai, Chuo-ku, Sagami-hara, Kanagawa 252-5210*

²*Department of Astronomy, Graduate School of Science, The University of Tokyo, 7-3-1 Hongo, Bunkyo-ku, Tokyo 113-0033*

³*Code 662, NASA/Goddard Space Flight Center, Greenbelt, MD 20771, USA*

⁴*Department of Physics, Graduate School of Science, Nagoya University, Furo-cho, Nagoya 464-8602*

⁵*Extra-Solar Planet Detection Project Office, National Astronomical Observatory of Japan,
2-21-1 Osawa, Mitaka, Tokyo 181-8588
ksaitou@astro.isas.jaxa.jp*

(Received 2011 April 1; accepted 2011 May 21)

Abstract

XSS J12270–4859 (J12270) is an enigmatic source of unknown nature. Previous studies revealed that the source has unusual X-ray temporal characteristics, including repetitive short-term flares followed by spectral hardening, non-periodic dips, and dichotomy in activity; i.e. intervals filled with flares and those without. Together with a power-law X-ray spectrum, it is suggested to be a low-mass X-ray binary (LMXB). In order to better understand the object, we present the results of our near-infrared (NIR) photometry and linear polarimetry observations as well as X-ray spectroscopy observations, which overlap with each other partially in time, taken respectively with the InfraRed Survey Facility (IRSF) and the Rossi X-ray Timing Explorer (RXTE). We detected several simultaneous NIR and X-ray flares for the first time. No significant NIR polarization was obtained. We assembled data taken with IRSF, RXTE, Suzaku, Swift, and other missions in the literature and compared the flare profile and the spectral energy distribution (SED) with some representative high-energy sources. Based on some similarities of the repetitive NIR and X-ray flaring characteristics and the broad SED, we argue that J12270 is reminiscent of microquasars with a synchrotron jet, which is at a very low luminosity state of $\approx 10^{-4}$ Eddington luminosity for a stellar mass black hole or neutron star at a reference distance of 1 kpc.

Key words: infrared: stars — stars: individual (XSS J12270–4859) — stars: variables: other — X-rays: stars

1. Introduction

XSS J12270–4859 (hereafter J12270) is one of the most mysterious X-ray objects among recent discoveries, which shows quite anomalous temporal characteristics both in the X-ray and optical regimes (Saitou et al. 2009; de Martino et al. 2010; Pretorius 2009). A possible association with the Fermi γ -ray source 1FGL J1227.9–4852 has also been proposed (de Martino et al. 2010; Stephen et al. 2010; Hill et al. 2011). It is conceivably a low mass X-ray binary (LMXB) from its rapid flux variation and a power-law spectrum in the X-ray (Saitou et al. 2009; de Martino et al. 2010), but conventional views of LMXBs are insufficient to explain its unusual features such as a broad spectral energy distribution (SED) up to GeV and anomalous X-ray variability.

To better understand the system, near-infrared (NIR) observations are key. Several spectral components are expected in the NIR regime for LMXBs, which include the thermal emission from the secondary star and outer part of the accretion disk, and non-thermal cyclo-synchrotron emission by electrons accelerated in a jet or hot inner accretion flow. These components have a dif-

ferent dependence on wavelengths and time variability (or lack thereof), thus comparison with NIR and other wavelength observations (Pretorius 2009; Saitou et al. 2009; de Martino et al. 2010) will help decompose the broad SED. Nevertheless, no results of targeted NIR observations have been presented to date for this source besides all-sky surveys.

The main purpose of this paper is to present the result of NIR photometry and linear polarimetry observations using the InfraRed Survey Facility (IRSF) 1.4 m telescope. During a part of our NIR observations, we also conducted simultaneous X-ray observations using the Rossi X-ray Timing Explorer (RXTE). In addition, we retrieve the unpublished archived X-ray data by the Swift satellite to complement the previous reports by Saitou et al. (2009) and de Martino et al. (2010) showing Suzaku, XMM-Newton, and RXTE data, and examine if these anomalous X-ray characteristics are common in this object.

The plan of this paper is as follows. In §2, we briefly review the previous observational findings of this object. In §3 and §4, we describe the observations and analysis of the data separately for each observing facility. In §5, we

combine all the results and discuss the possible nature of the system. The main results are summarized in §6.

2. Object Properties

J12270 was initially discovered in the RXTE slew survey (Revnivtsev et al. 2004) and later identified as a hard X-ray emitter by INTEGRAL (Bird et al. 2007; Bird et al. 2010). J12270 was once classified as an intermediate polar (IP), a binary system of a moderately magnetized ($\sim 10^{5-7}$ G) white dwarf and a late-type companion based on optical spectroscopy (Masetti et al. 2006) and a hint of 860 s X-ray periodicity (Butters et al. 2008).

The results of X-ray spectroscopy (Saitou et al. 2009; de Martino et al. 2010), however, argue against the IP nature of this source. The X-ray spectrum is featureless, not showing signature of Fe emission lines, contrary to the defining IP characteristic of strong Fe emission lines (Ezuka & Ishida 1999).

Anomalous X-ray temporal characteristics of J12270 were first discovered by Saitou et al. (2009) using the Suzaku X-ray satellite and later confirmed by de Martino et al. (2010) using the XMM-Newton satellite. The features include: (1) repetitive flux increase lasting for a short duration of a few hundred seconds (flares), (2) sudden flux decrease with no apparent periodicity (dips), (3) spectral hardening after some flux increase (hardening), and (4) dichotomy in X-ray activity; i.e. intervals filled with flares and those without. de Martino et al. (2010) also pointed out that there are two types of dips; i.e., dips with hardening only seen immediately after flares and those without hardening seen during quiescent phases without apparent periodicity.

Unique temporal characteristics were also reported in the optical and in the ultraviolet (UV) regimes. Pretorius (2009) found flux variation of a large amplitude (> 1 mag), which is accompanied by flickering and a distinctive pattern of variation. In optical spectroscopy, they also reported that the equivalent width of the H α emission line was twice as large as that reported by Masetti et al. (2006). Using the broad-band capability of XMM-Newton by combining the optical monitor (OM) and the X-ray CCD detectors, de Martino et al. (2010) accumulated many new results revealing intriguing features of this source: (1) optical/UV flares are seen, which are always accompanied by X-ray flares, (2) X-ray dips in the quiescent phase are not seen in the UV, and (3) a possible orbital period of 4.32 hour in V band photometry.

Hill et al. (2011) presented a detailed temporal and spectral analysis of the Fermi source, for which they claim J12270 to be the most likely counterpart. The 0.1–300 GeV light curve is stable with a 4-day time binning over 1 year. The 0.1–300 GeV luminosity is $\sim 4.9 \times 10^{33}$ erg s $^{-1}$ at an assumed distance of 1 kpc, which is comparable to that of X-ray luminosity in 0.2–12 keV band (Saitou et al. 2009). The spectrum is represented by a power-law model with a photon index of 2.5 and shows a significant cut-off at 4.1 GeV. Based on these properties, Hill et al. (2011) claimed that the Fermi source is a binary

millisecond pulsar.

Hill et al. (2011) also conducted radio imaging observations around the Fermi source using the Australian Telescope Compact Array (ATCA) and the Giant Metrewave Radio Telescope and found a radio counterpart to J12270. A significant detection was obtained at 5.5 and 9 GHz with a flux of 0.18 and 0.14 mJy, respectively. No millisecond pulsation was detected by follow-up observations using the Parkes telescope.

3. Observations and Data Reduction

3.1. IRSF

We had two runs of NIR observations in 2009 January and March with a total of 13 nights (table 1). We used IRSF 1.4 m telescope in the South African Astronomical Observatory. A part of the observations on March 13 and 15 was coordinated to be simultaneous with RXTE (§ 3.2). The NIR camera at the Cassegrain focus of the telescope has two modes of operation: photometry with the Simultaneous three-color InfraRed Imager for Unbiased Survey (SIRIUS: Nagashima et al. 1999; Nagayama et al. 2003) and linear polarimetry with the SIRIUS Polarimetry mode (SIRPOL: Kandori et al. 2006).

SIRIUS yields simultaneous J (1.25 μm), H (1.63 μm), and K_s (2.14 μm) band images using two dichroic mirrors. A very fast readout (5 s per frame) enables us to follow rapid flux changes of J12270 reported in the optical and X-rays. SIRIUS has 1024×1024 pixels with a pixel scale of $0''.45$ pixel $^{-1}$, making a $7''.7 \times 7''.7$ field of view (FoV).

SIRPOL is equipped with an achromatic (1–2.5 μm) wave plate rotator unit over SIRIUS and takes simultaneous J , H , and K_s band images at four position angles (0° , 45° , 22.5° , and 67.5°) for measurements of linear polarization. The Stokes parameters I , Q , and U are obtained as $I = (I_{0^\circ} + I_{45^\circ} + I_{22.5^\circ} + I_{67.5^\circ})/2$, $Q = I_{0^\circ} - I_{45^\circ}$, and $U = I_{22.5^\circ} - I_{67.5^\circ}$, where I_x is the intensity of an object at the position angle x . The polarization degree P and the polarization angle θ are then calculated as $P = \sqrt{Q^2 + U^2}/I$ and $\theta = 1/2 \arctan(U/Q)$.

All SIRIUS and SIRPOL observations were carried out with a 15 s exposure per frame with a 10-point dithering. The observing conditions were photometric with a typical seeing of $1''.4$. Dark frames were obtained at the end of each night, while twilight flat frames were obtained daily before and after the observation and averaged over a month.

We reduced the data following the standard pipeline procedure using the Imaging Reduction and Analysis Facility (IRAF) software package. The procedure includes subtracting dark frames, flat-fielding, masking bad pixels, and eliminating fringe patterns by OH emission and the reset anomaly of the detector. Ten dithered frames were then merged into one image. A small number of frames were discarded during the automated pipeline processing due to incompleteness of the data.

3.2. RXTE

We observed J12270 using RXTE (Bradt et al. 1993) twice on 2009 March 13 and 15 as a target of opportunity program to conduct simultaneous X-ray and NIR observations (table 1). Among three instruments onboard the satellite, we used the Proportional Counter Array (PCA: Jahoda et al. 2006), which consists of five Proportional Counter Units (PCUs). The PCA, which is a non-imaging detector with a $1^\circ \times 1^\circ$ FoV, covers an energy range of 2–60 keV and has a total area of 6250 cm².

We used the data obtained by the top layer of PCU 2 with a time resolution of 16 s. Following the standard prescription, we discarded events when the separation between the object and the satellite pointing was larger than 0°02 and the Earth elevation angle was below 10°. We further removed events during South Atlantic Anomaly passages and 30 min thereafter, those within 600 s before and 150 s after PCA breakdowns, and those when the electron to X-ray event ratio was larger than 0.1. As a result, the total exposure time was 16 ks (table 1). The source events are subject to contamination by other objects due to the lack of imaging capability and a large FoV of the instrument. We estimate the contamination to be $\sim 10\%$ by comparing the J12270 flux between RXTE and Suzaku (Saitou et al. 2009). We used the HEASoft¹ version 6.6 for the reduction of the RXTE data.

3.3. Swift

The Swift satellite (Gehrels et al. 2004) observed J12270 twice on 2005 September 15 and 24 (table 1). The X-Ray Telescope (XRT: Burrows et al. 2005) is equipped with an X-ray CCD device for imaging-spectroscopy, which has a sensitivity in an energy range of 0.2–10 keV, an energy resolution of 140 eV at 5.9 keV, an effective area of 125 cm² at 1.5 keV, and a FoV of 23'6 × 23'6. We used the photon counting mode with a frame time of 2.5 s.

The data were retrieved from the archive and reduced with the standard pipeline process, yielding a total exposure time of ~ 7 ks (table 1). We used the HEASoft version 6.5 for the reduction of the Swift data.

4. Analysis

4.1. IRSF

4.1.1. Photometry

We constructed NIR light curves using both SIRIUS and SIRPOL observations. J12270 was too faint to be detected in each frame exposed for 15 s, thus the minimum time resolution of the light curves is the time to take a set of 10 dithered frames. For the SIRPOL data, the Stokes I images were used. Because one I image requires four images at different position angles, the temporal resolution decreases by 1/4 plus overheads from the SIRIUS data (~ 230 s) to the SIRPOL data (~ 1355 s).

The astrometry was calibrated using 28 2MASS (Skrutskie et al. 2006) sources in the FoV, which are

Table 1. Log of the observations

Instrument	Sequence number	Obs. start (UT) Date*	Time [†]	$t_{\text{exp}}^{\ddagger}$ (ks)
<i>IRSF</i>				
SIRIUS	—	09-01-15	23:36	0.9
	—	09-01-16	22:33	0.5
	—	09-01-18	00:08	0.6
	—	09-01-19	00:32	0.6
	—	09-01-20	00:02	0.6
	—	09-01-20	23:15	0.6
	—	09-01-23	00:52	0.5
	—	09-03-12	01:25	4.1
SIRPOL	—	09-03-13	18:14	14.4
	—	09-03-17	17:58	20.0
	—	09-03-14	23:35	4.2
PCA	94416-01-01	09-03-15	18:38	8.4
		09-03-16	18:38	8.4
		09-03-13	20:06	9.7
<i>RXTE</i>				
PCA	94416-01-01	09-03-15	20:42	6.5
		09-03-15	20:42	6.5
<i>Swift</i>				
XRT	0035101001	05-09-15	00:22	4.9
	0035101002	05-09-24	06:09	1.9

* Date in the format of YY-MM-DD.

[†] Time in the format of hh:mm.

[‡] Net exposure time.

bright but not saturated in SIRIUS images. They are within a magnitude range of 12.0–15.5, 12.0–15.0, and 12.0–14.0 mag respectively in the J , H , and K_s band and with a magnitude error of ≤ 0.05 mag.

Aperture photometry was performed with a $2''.72$ (6 pixel) radius for the source and a $4''.53$ – $9''.05$ (10–20 pixel) annulus for the sky. The sources used as astrometric references were also used as relative photometric references, except that we excluded up to two sources showing a significant deviation from the phenomenological linear relation between 2MASS and SIRIUS or SIRPOL magnitudes in each band.

Figures 1a, 2a, and 3 show the NIR flux (J , H , and K_s) and color ($J-K_s$) light curves on March 13 (SIRIUS), 15 (SIRPOL), and 17 (SIRIUS), respectively. For the first two figures, the simultaneous X-ray light curves (§ 4.2) are displayed together. Several flares were clearly detected in conjunction with X-ray flares. Using all the SIRIUS data sets in table 1, we constructed a folded light curve at a claimed orbital period of 4.32 hr (de Martino et al. 2010). However, we could not confirm the period in the NIR bands.

4.1.2. Polarimetry

For the SIRPOL data, we performed aperture photometry for images taken at four different position angles following the same procedure with the SIRIUS photometry. We then calculated the Stokes parameters I , Q , and U , and derived the polarization degree P . The uncertainties of the Stokes parameters and the polarization degree were derived by propagating the photometric uncertainty of each source in images at each position angle. Systematic

¹ See <http://heasarc.gsfc.nasa.gov/docs/software/lheasoft/> for details.

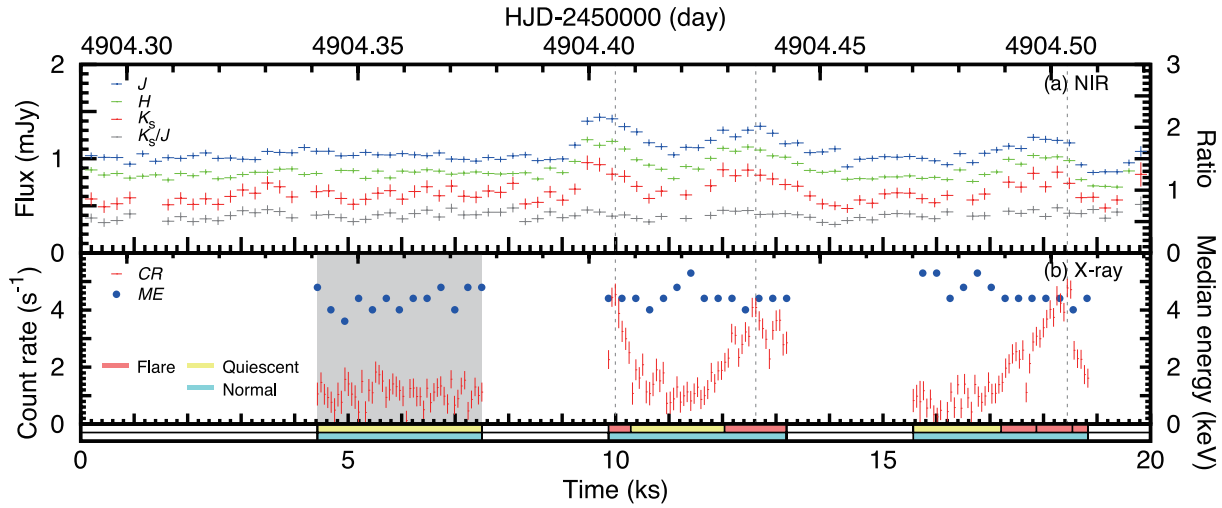


Fig. 1. Simultaneous NIR (SIRIUS) and X-ray light curves on 2009 March 13. The time is shown as Heliocentric Julian Date (HJD) on the top axis and in ks on the bottom axis. The origin of the abscissa is 4904.29 in HJD–2450000. (a) NIR light curves. The fluxes in J , H , and K_s bands (left axis) and the color defined as K_s/J (right axis) are respectively represented by blue, green, red, and gray cross points. A typical time bin is ~ 230 s. (b) X-ray light curves. The background-subtracted count rate (CR ; left axis) and median energy (ME ; right axis) are represented by red and blue circles, respectively. The CR is binned by 64 s, while the ME is binned by 256 s. The 1σ Poisson error is shown for the CR . The mean and standard deviation of CR and ME are derived from a quiescent interval with a gray shaded region. The Bayesian segments and their classifications are color-coded in the two horizontal bars at the bottom; flare (red) and quiescent (yellow) for the CR segments and normal (blue) for the ME segments. The vertical broken lines indicate the time of X-ray maximum in each flare.

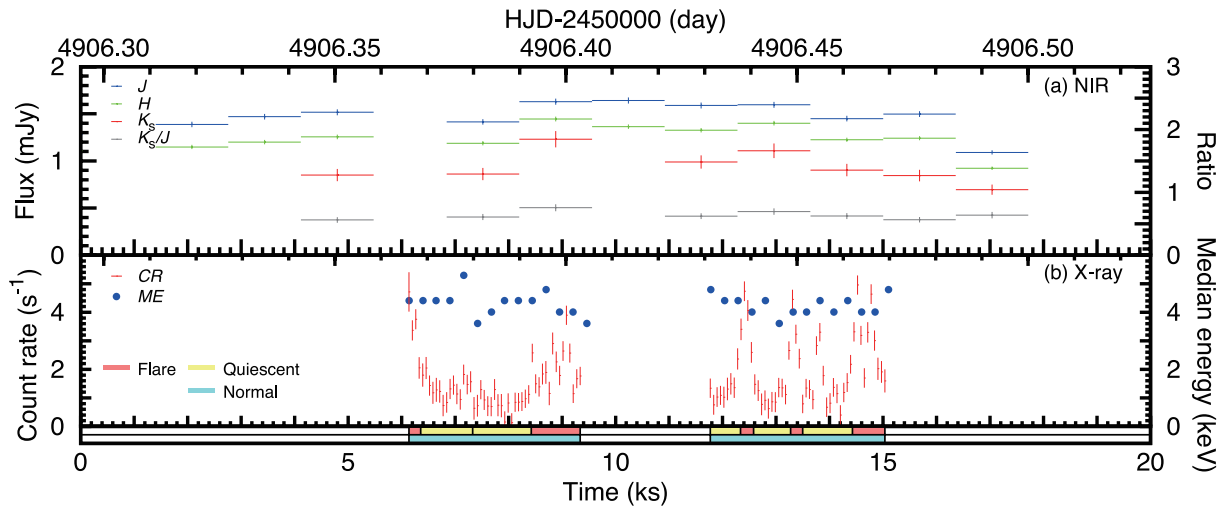


Fig. 2. Simultaneous NIR (SIRPOL) and X-ray light curves obtained on 2009 March 15. The origin of the abscissa is 4906.295 in HJD–2450000. A typical time bin of the NIR data is ~ 1355 s. Markings follow figure 1.

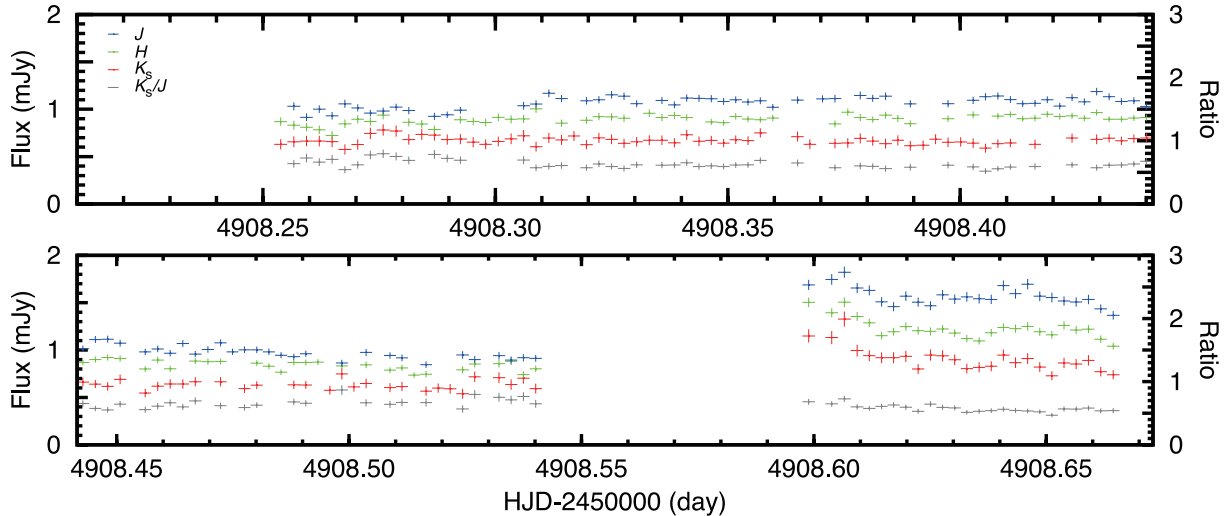


Fig. 3. NIR (SIRIUS) light curves obtained on 2009 March 17. The curves are folded by 20 ks. The origin of the abscissa is 4908.21 in HJD–2450000. Markings follow figure 1. A part of the observing time was lost in the latter half due to high humidity.

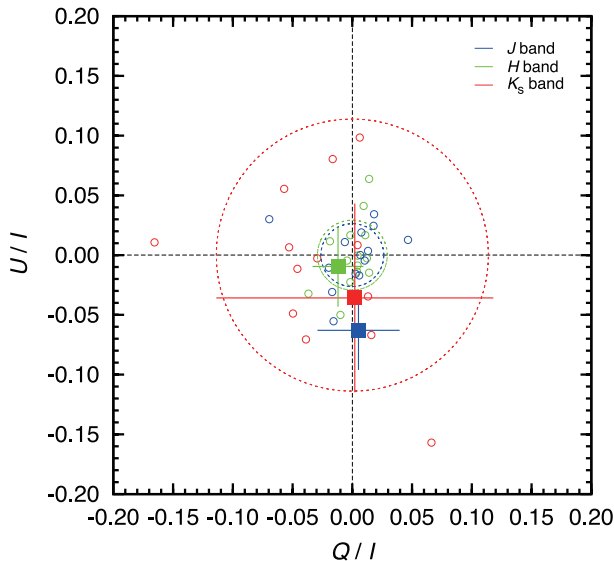


Fig. 4. Q/I versus U/I plot after offset correction. Large filled squares indicate J12270, while small open circles indicate comparison sources within ± 0.5 mag of J12270. For J12270, the 1σ statistical uncertainty is shown with error bars. The dotted circles indicate the standard deviation among the comparison sources, representing the systematic uncertainty of the origin. Different bands are represented by different colors.

offset in the polarization degree, which includes both instrumental artifacts and the global mean of the interstellar dust polarization in the direction of the object field, were derived (2.2–3.8%) and corrected using 14 2MASS sources within ± 0.5 mag of J12270 in each band.

Figure 4 shows the Q/I versus U/I plot of J12270 and the comparison sources. All SIRPOL data (table 1) were stacked. Assuming that the comparison sources have no intrinsic linear polarization, the statistical scatter was derived (dotted circles), which represents the uncertainty in

the offset correction in each band.

We consider that a significant linear polarization was not detected from J12270 in all bands, because (1) the polarization degree (distance from the origin in figure 4) is within a 2σ convolved uncertainty of the statistical uncertainty in photometry and the systematic uncertainty in the offset correction and (2) the polarization angle (the angle between the x -axis and the line connecting the origin and the data point) is not aligned in the three bands. A 1σ upper limit in the polarization degree was 11.4, 4.2, and 12.7% respectively in the J , H , and K_s bands. A significant polarization was not detected even if the data were limited only to those during flares.

4.2. RXTE

4.2.1. Light Curves

We constructed the X-ray light curve in the 2–10 keV band. The background rate was estimated using the PCA background model provided by the instrument team². Figures 1b and 2b show the background-subtracted count rate (CR) and the median energy (ME) respectively for the observations in 2009 March 13 and 15. The former observation overlaps partially with a SIRIUS observation, while the latter with a SIRPOL observation. The ME is a proxy for the conventional hardness ratio (Hong et al. 2004), which is better suited for low photon statistics and is defined as the median energy of all photon in a time interval³. The CR and the ME were binned with 64 and 256 s bin^{-1} , respectively.

Similarly to the Suzaku and XMM-Newton light curves (Saitou et al. 2009; de Martino et al. 2010), the RXTE

² See <http://heasarc.gsfc.nasa.gov/docs/xte/recipes/pcabackest.html> for details.

³ Strictly speaking, we calculated the median of the instrument channel and converted it to median energy using the energy-channel conversion table. See <http://heasarc.gsfc.nasa.gov/docs/xte/e-c-table.html> for details.

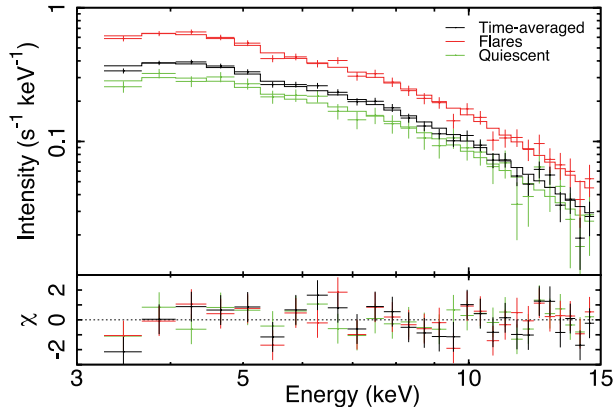


Fig. 5. RXTE background-subtracted spectra of all data (black) together with those during flare (red) and quiescent (green) phases. The upper panel shows the data (cross) and the best-fit model (solid line), while the lower panel shows the residuals to the fit.

light curves also show various types of variability both in *CR* and *ME*. We follow Saitou et al. (2009) for a quantitative assessment of the variation. First, we divided the *CR* and *ME* curves into “segments” with a constant value using the Bayesian blocks method (Scargle 1998). Second, we calculated the mean and the standard deviation of *CR* and *ME* in a featureless interval (the shaded region in figure 1b) to characterize the base levels. The mean and the standard deviation of the *CR* are 1.07 and 0.37 s⁻¹, respectively, while those of the *ME* are 4.34 and 0.39 keV, respectively. Finally, we classified the segments as (a) “dips” for segments with *CR* below the mean by more than 2 σ , (b) “flares” for those with *CR* above the mean by more than 2 σ , and (c) “quiescence” for the remainder in the *CR* segments, and (i) “hard” phase for those with *ME* above the mean by more than 2 σ and (ii) “normal” for the remainder in the *ME* segments. The segments are color-coded following the classification in figures 1b and 2b. We found some flares in both observations, but no dip and hard phases.

4.2.2. Spectra

We constructed background-subtracted spectra using all data, those only during the flare segments, and those only during the quiescent segments (figure 5). The background spectra were generated using the same method as for the temporal analysis (§ 4.2.1). No prominent feature was found. We fitted the 3–15 keV spectra with a power-law model attenuated by an interstellar absorption model (*tbabs*: Wilms et al. 2000). We fixed the absorption column density to the value 1.0×10^{21} cm⁻² derived from the Suzaku (Saitou et al. 2009) and the XMM-Newton (de Martino et al. 2010) spectra, as the lack of sensitivity below 2 keV in RXTE did not allow us to constrain the value. We obtained acceptable fits for the three spectra (table 2). The power-law index is almost compatible among the three, indicating that the differences are almost due to the changing flux.

Table 2. Best-fit spectral parameters.*

State	Γ^\dagger	F_X^\ddagger	χ_{red}^2 (dof) [§]
Time-averaged	$1.71^{+0.06}_{-0.06}$	$2.45^{+0.06}_{-0.06}$	1.06 (26)
Flares	$1.77^{+0.07}_{-0.07}$	$3.94^{+0.11}_{-0.11}$	0.83 (26)
Quiescent	$1.63^{+0.13}_{-0.13}$	$2.00^{+0.10}_{-0.11}$	0.52 (26)

* The errors are for 90% statistical uncertainty.

† Photon index of the power-law.

‡ The observed 3–15 keV flux in units of 10^{-11} erg s⁻¹ cm⁻².

§ The reduced χ^2 (χ_{red}^2) and the degrees of freedom (dof).

4.3. Swift

4.3.1. Light Curves

In the XRT images, the source events were extracted from a circle of a 47''1 (20 pixel) radius covering 90% of 1.5 keV photons for a point source, while the background events were taken from an annulus with inner and outer radii of 94''3 (40 pixel) and 176''8 (75 pixel), respectively. Some data were affected by photon pile-up, for which we excluded the central 7''1 circle (3 pixel) and rescaled the flux to compensate for the reduced aperture (Pagani et al. 2006).

Similarly to the RXTE data, we constructed the *CR* and *ME* light curves in 0.2–10 keV (figure 6). The *CR* and the *ME* were binned with 128 and 256 s bin⁻¹, respectively. We derived the mean and the standard deviation of *CR* as 0.26 ± 0.06 s⁻¹, and those of *ME* as 1.49 ± 0.21 keV, respectively, using featureless intervals (the shaded regions in figure 6). Swift data are composed of 13 snapshots of a very short exposure, so we did not employ the Bayesian blocks method for segmentation and classification of the variability. However, we do see some features similar to flares and hard phases as indicated respectively by red and blue arrows in figure 6.

5. Discussion

5.1. NIR Flares

Figure 1 convincingly shows that all X-ray flares accompany NIR flares. Figure 2 in de Martino et al. (2010) also shows that all X-ray flares accompany optical flares. It is of little doubt that all these phenomena are related to each other.

Looking closely into the flares, it is interesting to point out the following: (1) NIR flare peaks appear before the corresponding X-ray peak by $\sim 150 - 300$ s (shown by dotted lines in figure 1). The optical flare peaks are also seen before the X-ray peak on a similar time scale (de Martino et al. 2010). (2) No clear change in NIR color is seen during the flares. The $J-K_s$ curve in figure 1 is consistent with being constant in a χ^2 test. (3) The amplification from the quiescent level is roughly the same among all NIR flares, which is also the case for X-ray flares.

Apart from the flux changes associated with X-ray flares, there is also a change in NIR flux by 0.5 mag between the third and fourth quarters in figure 3. In comparison to other sources used as photometric reference, we found that this phenomenon is unique to J12270. It

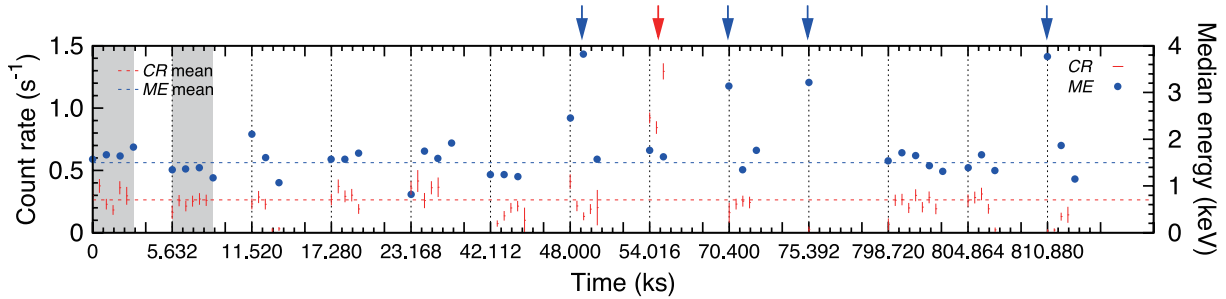


Fig. 6. Swift light curves of the *CR* and the *ME*. Markings follow figure 1. The origin of the time represents 3628.51409 d in HJD–2450000. Since the Swift observations are short and discontinuous, we only present the intervals with data and their start time. Red and blue arrows on the top axis indicate possible flares and hard phases, respectively. The horizontal broken lines represent the mean of the *CR* and the *ME* derived from the data in the shaded intervals.

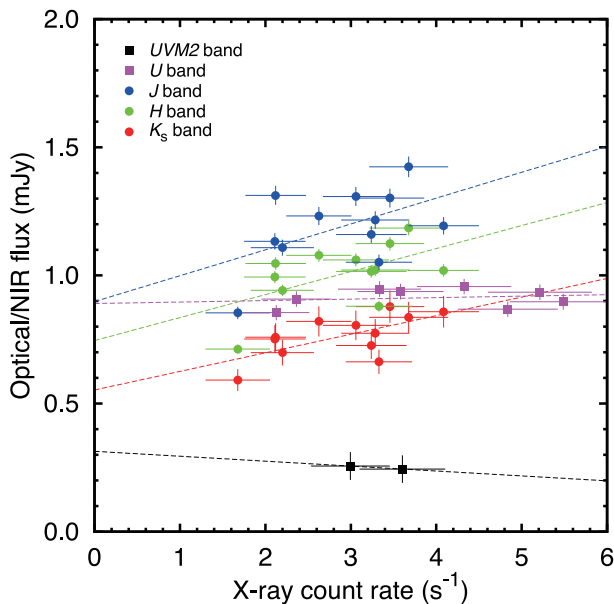


Fig. 7. X-ray count rate (2–10 keV) versus NIR (*J*, *H*, and *K_s*) or optical (*U* and *UVM2*) flux during flares. Different bands in the NIR and optical are shown in different colors. The dotted lines are the linear regression of the relation. The simultaneous RXTE X-ray and NIR data (this work) and XMM-Newton X-ray and optical data (de Martino et al. 2010) are used.

is either that the quiescent base level has changed or that the fourth quarter was observed during a decay phase of a long flare.

In order to separate the variable and non-variable components in the NIR, we plotted X-ray count rate versus NIR flux in the flare segments separately for the *J*, *H*, and *K_s* bands in figure 7. We used a larger time bin of 300 s to accommodate a possible time lag between the X-ray and NIR flares. The X-ray and NIR fluxes are roughly proportional, yielding acceptable fits by a linear relation for the three bands. The slopes of the three linear relations are consistent with each other, which is consistent with the NIR flares being colorless. Assuming that the y-intercept of the linear relations is the residual non-variable component in the NIR flux, it is estimated as 0.90, 0.75,

and 0.55 mJy in *J*, *H*, and *K_s* band, respectively. The contamination to the X-ray flux by other sources (§ 3.2) changes this estimate by $\lesssim 10\%$.

When we add the optical data taken from de Martino et al. (2010) in figure 7, a different and nearly flat slope is found for the optical photometry against the X-ray count rate during the flare. This might indicate that there are two components in the NIR and optical bands; one is non-variable during flares and is more intense in the optical band, while the other is variable during flares with a proportional behavior to X-ray counts and is more intense in the NIR band.

A plausible origin of the non-variable component is the emission from the secondary star and a part of the accretion disk, if J12270 is indeed a LMXB. If we assume that the non-variable NIR flux is entirely from the secondary, we can give a crude constraint to the spectral type of the companion. By dereddening the NIR color using the X-ray absorption $N_{\text{H}} = 1.0 \times 10^{21} \text{ cm}^{-2}$ and the conversion ratio of $N_{\text{H}}/A_{\text{V}} = 1.79 \times 10^{21} \text{ cm}^{-2} \text{ mag}^{-1}$ (Predehl & Schmitt 1995), we estimate the spectral type of the secondary to be F5 V–F7 V if it is a dwarf and K2 III if it is a giant (Tokunaga 2000). The distance is then estimated as ~ 1.6 kpc (dwarf) or ~ 18 kpc (giant). The distance for the giant is too large, putting this source at the edge or beyond our Galaxy. Therefore, it is more likely that the secondary is a red dwarf. de Martino et al. (2010) derived the secondary mass as $M_2 = 0.3\text{--}0.4 M_{\odot}$ independently using an empirical dynamical relation between the orbital period and M_2 , which is slightly smaller than our estimate of $\sim 1.4 M_{\odot}$. In any case, the spectral type determined only from NIR flux should be taken with caution. NIR spectroscopic observations are required to decompose the possible secondary and disk emission and to derive on accurate spectral type of the secondary (e.g., Bandyopadhyay et al. 1997).

Because the distance is so poorly constrained with the currently available data set, we normalize physical values with a 1 kpc distance hereafter. The distance does not contradict the observed N_{H} value and its Galactic position. The height from the Galactic plane would be 240 pc at a 1 kpc distance, which is not exceptionally large considering that some LMXBs lie beyond this height

(e.g., XTE J1118+480 at 1.5 kpc; Mikolajewska et al. 2005; Gelino et al. 2006). An extrapolated X-ray luminosity using the RXTE result (table 2) is $L_{X(0.1-100 \text{ keV})} \sim 1 \times 10^{34} (d/1 \text{ kpc})^2 \text{ erg s}^{-1}$. Combining a γ -ray luminosity of $L_{\gamma(0.1-300 \text{ GeV})} \sim 5 \times 10^{33} (d/1 \text{ kpc})^2 \text{ erg s}^{-1}$ (Hill et al. 2011), we derived the bolometric luminosity as an order of $\sim 10^{34} (d/1 \text{ kpc})^2 \text{ erg s}^{-1}$, which means that this source is in a very low luminosity state with $\approx 10^{-4}$ of the Eddington luminosity for a stellar mass black hole or neutron star.

5.2. NIR Polarization

Some LMXBs, particularly black hole binaries in a low luminosity state, are often accompanied by relativistic jets (Fender 2006). Synchrotron radiation is emitted over a wide spectral range. Some evidence suggests that a break occurs between the optically-thin and optically-thick synchrotron emission around the NIR band (e.g. Fender 2006). It is also expected that the contrast of the synchrotron emission is relatively high against other spectral component in this band. Therefore, many efforts have been made to detect linear NIR polarization from many LMXBs (Dubus & Chaty 2006; Shahbaz et al. 2008; Russell & Fender 2008), which would argue for synchrotron origin of the NIR emission.

However, only two sources (Sco X-1 and GRO J1655–40; Russell & Fender 2008) were detected with NIR polarization intrinsic to the source. The polarization degree was a few percent at most, which is smaller than our upper limit for J12270 (§ 4.1.2). Our observation was not sensitive enough to probe possible linear polarization, and the lack of detection should not discourage further investigation.

5.3. Long-term X-ray Behavior

We have looked into all the X-ray data available to date through Butters et al. (2008), Saitou et al. (2009), de Martino et al. (2010), and this work using the Suzaku, XMM-Newton, RXTE, and Swift satellites over a span of 3.5 years starting in 2007 November with a total integration of 133 ks. The anomalous temporal behavior is seen in all the data sets. The best-fit parameters in the X-ray spectral fitting during flares and those outside of flares are almost the same in all data. Also, light curves in several X-ray bands are available from 2009 August up to the time of writing, from the Monitor of All-sky X-ray Imager onboard the International Space Station⁴, which are stable with no apparent phase changes seen in other monitored LMXBs. All these suggest that the X-ray characteristics presented in previous and this work are the norm of this object.

Hill et al. (2011) claim that the Fermi source, for which J12270 is the most likely counterpart, is a millisecond pulsar, although the optical observation conducted in 2008 July (Pretorius 2009) clearly shows a signature of accretion. To reconcile this inconsistency, they speculated

that the system changed from accretion-powered phase to rotation-powered phase before the Fermi observation in 2008 August to 2010 September. However, we consider this to be unlikely because the X-ray results throughout this period show no significant changes in its spectral and temporal characteristics of the source.

5.4. X-ray Flares

With a close inspection of X-ray flares, some features are seen commonly in all events: (1) a time profile of slow rise and rapid decay, (2) the constant contrast between the flare peak and the base level, (3) no spectral changes during flares, (4) undershoot in flux and spectral hardening after flares, which are most notably seen in the last flare in a series of repetitive flares, and (5) simultaneous optical and NIR flares and their flare peaks before an X-ray flare peaks.

A difference among these flares is the time scale of the profile. To test this idea, we used one of the XMM-Newton flares (de Martino et al. 2010) as a template and fitted all the other X-ray flares by thawing the time scale. Figure 8 (a–d) shows the result, in which we present the template flare profile (a) and three other flares (b–d) scaled with the best-fit time scaling factor. We found that the profiles are similar to each other, including the development in the spectral hardness and optical/NIR flux.

The repetitive nature of such X-ray flares is a distinctive character of J12270. We compare the flare profile with other classes of Galactic sources showing repetitive flares and having either a black hole or a neutron star in the system (figure 8). We pick up representative sources from each class; (e) GRS 1915+105 for microquasars (Belloni et al. 2000), (f) 4U 1728–34 for type I bursters (van Straaten et al. 2001), (g) MXB 1730–335 for type II bursters (Lewin et al. 1976), and (h) Sgr A* (Porquet et al. 2003). GRS 1915+105 is known to show a wide variety of flare phenomenology. We compared with the class β variation in a phenomenological classification scheme by Belloni et al. (2000).

de Martino et al. (2010) argued that J12270 is unlikely to be a type I and type II burster. Type I bursters are characterized by rapid flux increase and slow exponential decay in their flare profile (figure 8f) and show clear X-ray spectral changes during flares. Type II bursters show a correlation between the flare energy and the waiting time for the flare. Both of these defining characteristics are not seen in J12270, ruling out the possibility that J12270 is either type I or type II bursters.

We consider that the similarities between J12270 and GRS 1915+105 (class β variation in Belloni et al. 2000) may be more relevant for unveiling the nature of this source. Both show repetitive flares in similar shapes but with slightly varying time scales, simultaneous NIR flares (Eikenberry et al. 1998), no spectral changes during flares, flux undershoot and spectral hardening after flares, most noticeably in the last flare in a series, and dichotomy between time intervals filled with flares and those without. There are some differences; e.g., a precursor flare is seen before a series of repetitive flares

⁴ See http://maxi.riken.jp/top/maxi_data/star_data/J1227-488/J1227-488.00055058g.lc.png for the latest data.

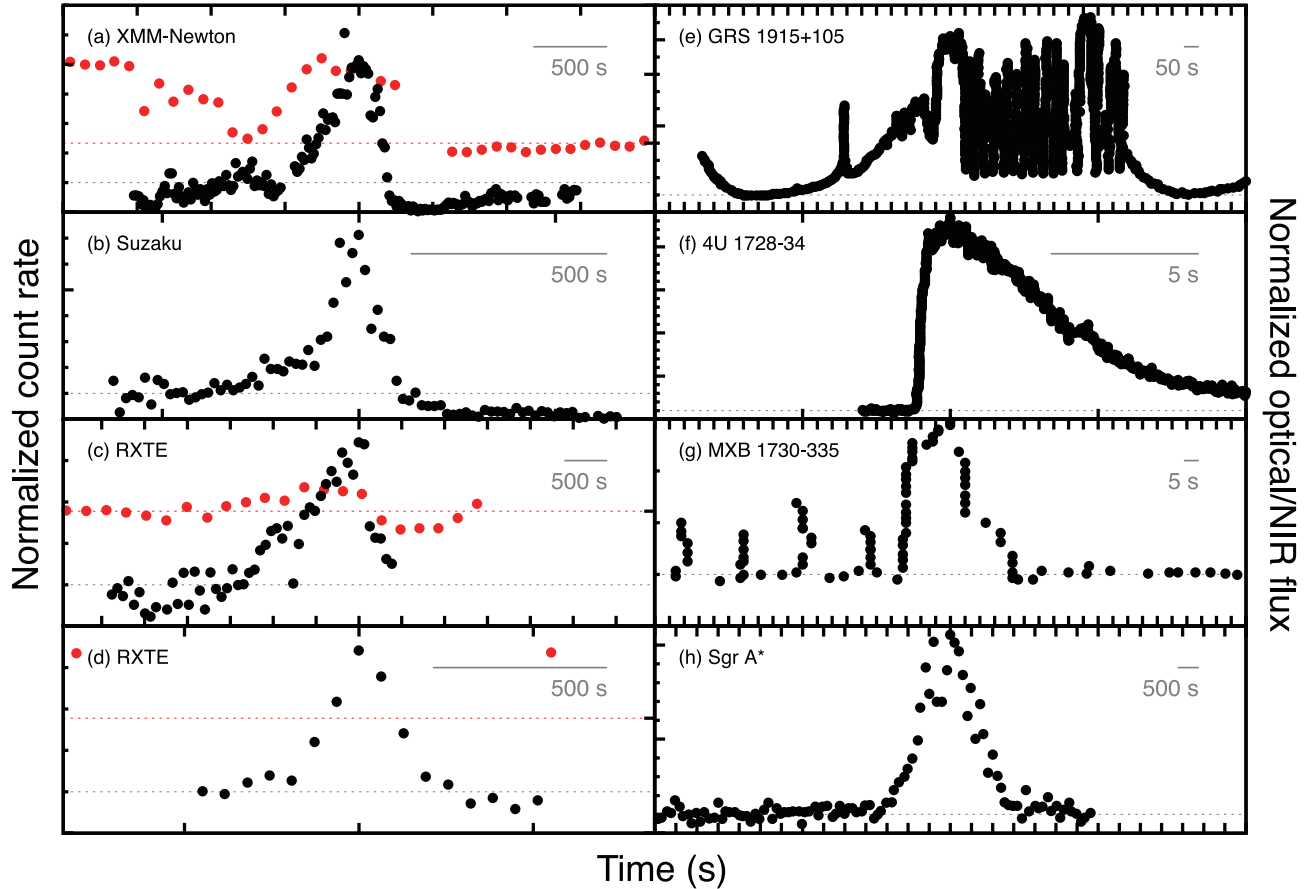


Fig. 8. Flare profiles of (a–d) J12270 in comparison with those in other X-ray sources showing repetitive flares: (e) a microquasar (GRS 1915+105 in the class β variation; Belloni et al. 2000), (f) a type I burster (4U 1728–34; van Straaten et al. 2001), (g) a type II burster (MXB 1730–335 a.k.a. the Rapid Burster; Lewin et al. 1976), and (h) Sgr A* (Porquet et al. 2003). The flare samples of J12270 are taken at (a) 4837.19, (b) 4687.82, (c) 4904.50, and (d) 4906.44 in HJD–2450000. Black points represent the X-ray count rate for all sources, while red circles represent optical/NIR flux for J12270. The scales are arbitrarily expanded to facilitate comparison. The abscissae are ticked by 500 s for (a–d, h), by 50 s for (e), and by 5 s for (f–g), while the ordinates are ticked with the quiescent level of being unity. The quiescent level, shown with the horizontal dotted line, is measured from a non-flaring period.

in GRS 1915+105, while no such feature is apparent in J12270. Also, GRS 1915+105 is known to have lots of other states (Belloni et al. 2000), while J12270 is known to have only one so far. GRS 1915+105 is close to the Eddington luminosity while J12270 is probably at very low luminosity. Despite these differences, it is interesting that many distinctive features of J12270 are also seen in GRS 1915+105.

One interesting source that may bridge between the two is IGR J17091–3624 (Altamirano et al. 2011a; Altamirano et al. 2011b). This source also shows repetitive flares in a similar time scale and a similar amplitude. The variation is reminiscent of the β class variation in GRS 1915+105 (Belloni et al. 2000), but the luminosity is nowhere near the Eddington limit. This may indicate that the anomalous flux variation seen in the three samples can occur at any luminosity.

Based on this, we speculate that the underlying physics to cause such X-ray variability is the same. The cause for the variability is not well understood for GRS 1915+105, let alone J12270. At least, we speculate two things:

- (1) The NIR flare peaks 150–300 s before X-ray peaks excludes the possibility of X-ray reprocessing to be the origin of the NIR flares.
- (2) The time scale of the flares in J12270 is much longer than the scales that are considered to be caused by jet ejection in other microquasars (e.g., GX 339–4 and XTE J1118+480; Casella et al. 2010; Gandhi et al. 2010; Kanbach et al. 2001). This suggests that the X-ray and NIR variability is not caused by jet ejection itself, but some sort of outside-in instability in the accretion disk or an extended corona. In fact, the flare peak delay between NIR and X-ray (§5.1) is comparable with the dynamical time scale of ~ 150 s for a $5 M_{\odot}$ black hole at a $10^4 r_g$ or ~ 170 s for a $1.4 M_{\odot}$ compact object at a $2.5 \times 10^4 r_g$, in which r_g is the gravitational radii.

5.5. Spectral Energy Distribution

It is vital to construct an SED to understand the nature of high-energy objects. To extend the SED shown in de Martino et al. (2010) to longer wavelengths, we retrieved survey data at many wavelengths, which include the Sydney University Molonglo Sky Survey (SUMSS;

Mauch et al. 2003) at 843 MHz, the AKARI all-sky survey in far-infrared at 160, 140, 90, and 65 μm (Yamamura et al. 2010) and in mid-infrared at 18 and 9 μm (Ishihara et al. 2010), the 2MASS all-sky survey catalogue (Skrutskie et al. 2006) in NIR, the US Naval Observatory catalogue (USNO-B; Monet et al. 2003) in the optical, the fourth IBIS/ISGRI soft gamma-ray survey catalog (Bird et al. 2010), and the Fermi Large Area Telescope first source catalogue (Abdo et al. 2010). We also added the recent ATCA radio detection at 5.5 and 9.0 GHz by Hill et al. (2011). We made an SED for observed as well as extinction-corrected fluxes using bands with a significant detection (figure 9 top). We found only upper limits for the SUMSS and AKARI data, which are indicated by downward arrows.

As a comparison, we present the SED of some microquasars: GRS 1915+105, XTE J1118+480, and Cygnus X-3 (figure 9 bottom). In the lower energy band, J12270 shares a common characteristic with the other microquasars, in which a nearly flat SED is seen down to ~ 1 GHz. This is interpreted as optically-thick synchrotron emission from relativistic jets (Blandford & Königl 1979).

In the upper energy band, the γ -ray spectrum of J12270 is apparently steeper and lower than its extrapolated X-ray spectrum. However, we can fit the X-ray to GeV SED with a simple broken power-law model with a break at $\sim 2 \times 10^{12}$ GHz (figure 9). The break at $\sim 10^{11}$ GHz for microquasars is expected and interpreted as the consequence of the synchrotron cooling in the optically-thin regime of the emission. The break frequency ν_{max} is determined from the balance between the radiative cooling and acceleration of electrons. If Fermi acceleration in shock waves is responsible for the acceleration,

$$\nu_{\text{max}} = 1.2 \times 10^{11} \left(\frac{\xi}{100} \right)^{-1} \left(\frac{v_{\text{shock}}}{c} \right)^2 \text{ [GHz]},$$

where v_{shock} is the shock velocity and ξ is the dimensionless parameter to represent the turbulence in the magnetic field in the shock; i.e., mean free path of an electron in units of the Larmor radius (Markoff et al. 2001).

Due to the break, microquasars are just below the sensitivity of the Fermi survey (Abdo et al. 2010). However, with a slight change in the parameters, a Fermi detection is not a surprise for microquasars. Indeed, the first such detection was reported from Cygnus X-3 recently by Corbel et al. (2010). J12270 shows a break at a frequency higher by a decade, which may indicate that it has a slightly more efficient acceleration in comparison to others, if it is a microquasar.

On the other hand, no AKARI detection and the ATCA detection below back-extrapolating the X-ray power-law (figure 9) suggest that there is a second break to the broadband power-law emission. In fact, a break in IR band attributed to the jet is observed in a microquasar GX 339-4 (Corbel & Fender 2002). Those two breaks at high energy and IR bands are reported in a black hole candidate XTE J1118+480 in the low/hard state (Markoff et al. 2001), whose emission is considered to be mainly came from synchrotron jet.

6. Summary

We conducted NIR and X-ray observations of the enigmatic source XSS J12270-4859. During the coordinated NIR and X-ray observations using IRSF SIRIUS and RXTE PCA, we detected simultaneous and repetitive NIR and X-ray flares for the first time. NIR polarization was not detected. Based on the observed data together with those presented in previous work (Saitou et al. 2009; de Martino et al. 2010), we compared the flare profiles and the SED with other classes of X-ray sources and argued that J12270 shows similarities with a type of variation seen in the microquasar GRS 1915+105 in many of its defining characteristics. Based on this and the broad SED commonly seen in microquasars, we argued that the nature of J12270 is a microquasar. At an assumed distance of 1 kpc, it has a very low luminosity of $\approx 10^{-4}$ of the Eddington luminosity for a stellar mass black hole or neutron star. If J12270 is confirmed to be a LMXB with a Fermi counterpart, it will be the first example of a γ -ray binary having a low-mass companion.

We thank Daisuke Kato for his help in obtaining NIR data for a SIRIUS run, Hirofumi Hatano for advice in polarimetry data reduction, Shinki Oyabu for advice on AKARI survey data, and Hajime Inoue and Mamoru Doi for useful discussion. We appreciate the telescope managers of RXTE for allocating a telescope time for our observation. K. S. is financially supported by the Japan Society for the Promotion of Science and the Hayakawa foundation of the Astronomical Society of Japan.

This research made use of data obtained from Data Archives and Transmission System (DARTS), provided by Center for Science-satellite Operation and Data Archives (C-SODA) at ISAS/JAXA, and from the High Energy Astrophysics Science Archive Research Center Online Service, provided by the NASA/Goddard Space Flight Center. We also made use of the SIMBAD database, operated at CDS, Strasbourg, France. IRAF is distributed by the National Optical Astronomy Observatories, which are operated by the Association of Universities for Research in Astronomy, Inc., under cooperative agreement with the National Science Foundation.

References

- Abdo, A. A., et al. 2010, *ApJS*, 188, 405
- Altamirano, D., et al. 2011a, *ATel*, 3230, 1
- Altamirano, D., et al. 2011b, *ATel*, 3299, 1
- Bandyopadhyay, R., Shahbaz, T., Charles, P. A., van Kerkwijk, M. H., & Naylor, T. 1997, *MNRAS*, 285, 718
- Belloni, T., Klein-Wolt, M., Méndez, M., van der Klis, M., & van Paradijs, J. 2000, *A&A*, 355, 271
- Bird, A. J., et al. 2007, *ApJS*, 170, 175
- Bird, A. J., et al. 2010, *ApJS*, 186, 1
- Blandford, R. D., & Königl, A. 1979, *ApJ*, 232, 34
- Bradt, H. V., Rothschild, R. E., & Swank, J. H. 1993, *A&AS*, 93, 355
- Burrows, D. N., et al. 2005, *Space Sci. Rev.*, 120, 165

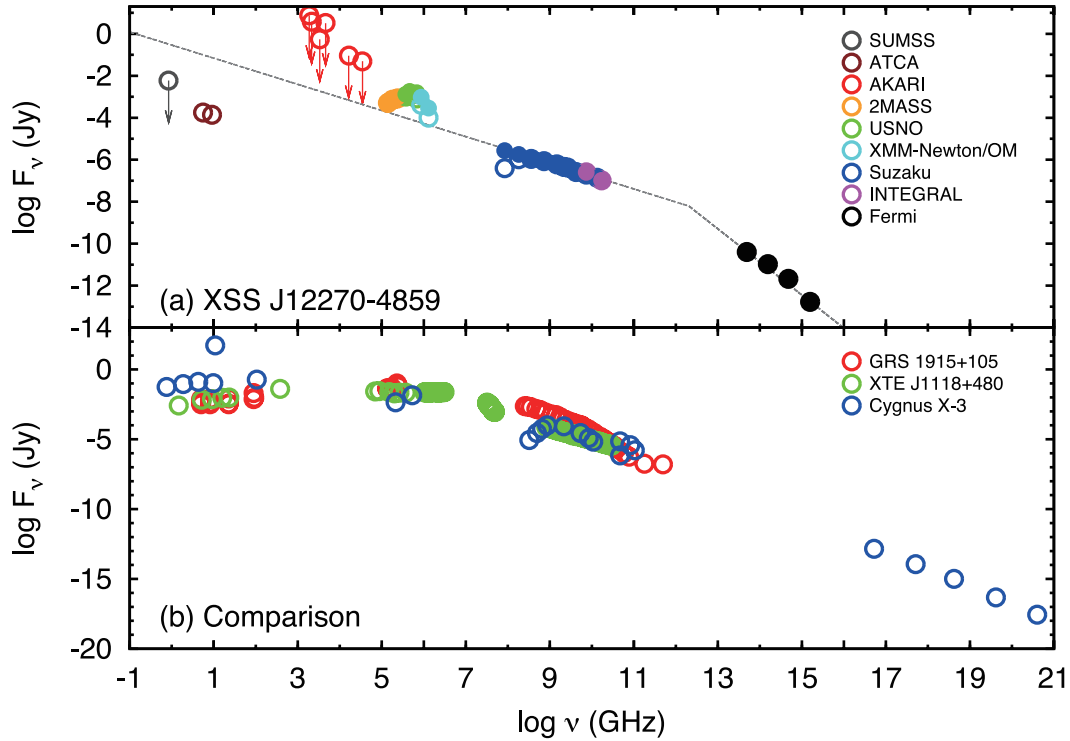


Fig. 9. SED of (a) J12270 in comparison with (b) some microquasars. (a) Open symbols indicate observed flux, while filled symbols indicate extinction-corrected flux. For the SUMSS and AKARI data, only upper limits are given, which are indicated by downward arrows. The broken lines represent extrapolated power-law model derived from the Suzaku or Fermi data. (b) The data are taken from Ueda et al. (2002) for GRS 1915+105, Markoff et al. (2001) for XTE J1118+480, and Sinitsyna et al. (2009) for Cygnus X-3 regardless of their states.

- Butters, O. W., Norton, A. J., Hakala, P., Mukai, K., & Barlow, E. J. 2008, *A&A*, 487, 276
- Casella, P., et al. 2010, *MNRAS*, 404, L21
- Corbel, S., & Fender, R. P. 2002, *ApJ*, 573, L35
- Corbel, S., & Fermi Large Area Telescope Collaboration 2010, *ATel*, 2611, 1
- de Martino, D., et al. 2010, *A&A*, 515, A25
- Dubus, G. & Chaty, S. 2006, *A&A*, 458, 591
- Eikenberry, S. S., Matthews, K. M., Morgan, E. H., Remillard, R. A., & Nelson, R. W. 1998, *ApJ*, 494, L61
- Ezuka, H. & Ishida, M. 1999, *ApJS*, 120, 277
- Fender, R. 2006, in *Compact Stellar X-Ray Sources*, ed. W. H. G. Lewin & M. van der Klis (Cambridge: Cambridge University Press), 381
- Gandhi, P., et al. 2010, *MNRAS*, 407, 2166
- Gehrels, N., et al. 2004, *ApJ*, 611, 1005
- Gelino, D. M., Balman, Ş, Kızıloğlu, Ü, Yılmaz, A., Kalemci, E., & Tomisick, J. A. 2006, *ApJ*, 642, 438
- Hill, A. B., et al. 2011, *MNRAS*, in press (arXiv:1103.2637)
- Hong, J., Schlegel, E. M., & Grindlay, J. E. 2004, *ApJ*, 614, 508
- Ishihara, D., et al. 2010, *A&A*, 514, A1
- Jahoda, K., et al. 2006, *ApJS*, 163, 401
- Kanbach, G., Straubmeier, C., Spruit, H. C., & Belloni, T. 2001, *Nature*, 414, 180
- Kandori, R., et al. 2006, *Proc. SPIE*, 6269, Ground-based and Airborne Instrumentation for Astronomy, ed. I. S. McLean & M. Iye (Bellingham, WA: SPIE), 159
- Lewin, W. H. G., et al. 1976, *ApJ*, 207, L95
- Markoff, S., Falcke, H., & Fender, R. 2001, *A&A*, 372, L25
- Masetti, N., et al. 2006, *A&A*, 459, 21
- Mauch, T., Murphy, T., Buttery, H. J., Curran, J., Hunstead, R. W., Piestrzynski, B., Robertson, J. G., & Sadler, E. M. 2003, *MNRAS*, 342, 1117
- Mikołajewska, J., Rutkowski, A., Gonçalves, D. R., & Szostek, A. 2005, *MNRAS*, 362, L13
- Monet, D. G., et al. 2005, *AJ*, 125, 984
- Nagashima, C., et al. 1999, in *Star Formation*, ed. T. Nakamoto (Nobeyama: Nobeyama Radio Observatory), 397
- Nagayama, T., et al. 2003, *Proc. SPIE*, 4841, Instrument Design and Performance for Optical/Infrared Ground-based Telescopes, ed. M. Iye & A. F. M. Moorwood (Bellingham, WA: SPIE), 459
- Pagani, C., et al. 2006, *ApJ*, 645, 1315
- Porquet, D., Predehl, P., Aschenbach, B., Grosso, N., Goldwurm, A., Goldoni, P., Warwick, R. S., & Decourchelle, A. 2003, *A&A*, 407, L17
- Predehl, P., & Schmitt, J. H. M. M. 1995, *A&A*, 293, 889
- Pretorius, M. L. 2009, *MNRAS*, 395, 386
- Revnivtsev, M., Sazonov, S., Jahoda, K., & Gilfanov, M. 2004, *A&A*, 418, 927
- Russell, D. M., & Fender, R. P. 2008, *MNRAS*, 387, 713
- Saitou, K., Tsujimoto, M., Ebisawa, K., & Ishida, M. 2009, *PASJ*, 61, L13
- Scargle, J. D. 1998, *ApJ*, 504, 405
- Shahbaz, T., Fender, R. P., Watson, C. A., & O'Brien, K. 2008, *ApJ*, 672, 510
- Sinitsyna, V. G., Alaverdian, A. Y., Mirzafatikhov, R. M., Musin, F. I., Nikolsky, S. I., Sinitsyna, V. Y., & Platonov, G. F. 2009, *Nuclear Physics B Proceedings*

Supplements, 196, 433

Skrutskie, M. F., et al. 2006, *AJ*, 131, 1163

Stephen, J. B., Bassani, L., Landi, R., Malizia, A., Sguera, V.,
Bazzano, A., & Masetti, N. 2010, *MNRAS*, 408, 422

Tokunaga, A. T. 2000, in *Allen's Astrophysical Quantities 4th*
ed., ed. N. Cox (New York: AIP Press, Springer), 143

Ueda, Y., et al. 2002, *ApJ*, 571, 918

van Straaten, S., van der Klis, M., Kuulkers, E., & Méndez, M.
2001, *ApJ*, 551, 907

Wilms, J., Allen, A., & McCray, R. 2000, *ApJ*, 542, 914

Yamamura, I., Makiuti, S., Ikeda, N., Fukuda, Y., Oyabu, S.,
Koga, T., & White, G. J. 2010, *AKARI-FIS Bright Source*
Catalogue Release note Version 1.0, ISAS/JAXA